

000  
001  
002  
003  
004  
005  
006  
007  
008  
009  
010  
011  
012  
013  
014  
015  
016  
017  
018  
019  
020  
021  
022  
023  
024  
025  
026  
027  
028  
029  
030  
031  
032  
033  
034  
035  
036  
037  
038  
039  
040  
041  
042  
043  
044  
045  
046  
047  
048  
049  
050  
051  
052  
053  

# REASONING IN SPACE VIA GROUNDING IN THE WORLD

**Anonymous authors**

Paper under double-blind review

## ABSTRACT

In this paper, we claim that 3D visual grounding is [one of the cornerstones](#) of spatial reasoning and introduce the *Grounded-Spatial Reasoner (GS-Reasoner)* to explore the effective spatial representations that bridge the gap between them. Existing 3D LLMs suffer from the absence of a unified 3D representation capable of jointly capturing semantic and geometric information. This deficiency is manifested either in poor performance on grounding or in an excessive reliance on external modules, ultimately hindering the seamless integration of grounding and spatial reasoning. To address this, we propose a simple yet effective *dual-path pooling* mechanism that tightly aligns geometric features with both semantic and positional cues, constructing a unified image patch-based 3D representation that encapsulates all essential information without increasing the number of input tokens. Leveraging this holistic representation, GS-Reasoner is the first 3D LLM that achieves autoregressive grounding entirely without external modules while delivering performance comparable to state-of-the-art models, establishing a unified and self-contained framework for 3D spatial reasoning. To further bridge grounding and spatial reasoning, we introduce the *Grounded Chain-of-Thought (GCoT)* dataset. This dataset is meticulously curated to include both 3D bounding box annotations for objects referenced in reasoning questions and step-by-step reasoning paths that integrate grounding as a core component of the problem-solving process. Extensive experiments demonstrate that GS-Reasoner achieves impressive results on 3D visual grounding, which in turn significantly enhances its spatial reasoning capabilities, leading to state-of-the-art performance.

## 1 INTRODUCTION

Visual-spatial intelligence encompasses the capability to perceive, interpret, and reason about 3D spaces, including the spatial layouts, object sizes, positions and their potential interactions. This skill is fundamental to various domains, such as embodied intelligence and autonomous driving. Accurately linking 3D objects with textual descriptions, a task known as 3D visual grounding, is a prerequisite for effective spatial reasoning. This aligns with human cognitive processes, where identifying relevant objects is a fundamental step before reasoning about their spatial relationships. Despite recent advancements in 3D large language models (LLMs) ([Cheng et al., 2024](#); [Cai et al., 2024](#); [Zhou et al., 2025](#); [Zheng et al., 2025](#); [Wang et al., 2025b](#); [Hong et al., 2023a](#); [Chen et al., 2024a](#); [Huang et al., 2023b](#); [2024](#); [Zhu et al., 2024b](#)), 3D LLMs still rely on pretrained 3D detectors or external decoders for grounding. This reliance not only limits their ability to fully understand 3D scenes but also impedes the cohesive integration of grounding and spatial reasoning. Therefore, a critical question arises: **How can we enable 3D LLMs to perform natural and effective grounding in an autoregressive manner, thereby enhancing their spatial reasoning capabilities?**

We identify two primary challenges in grounding enhanced spatial reasoning. The first challenge arises from the inherent complexity of 3D data. Unlike 2D images, point cloud-based 3D scenes encode rich spatial relations and depth cues that are difficult to capture and align with the semantic space of LLMs, especially given the scarcity of large-scale 3D datasets. Moreover, representing such fine-grained structures often requires a substantially larger number of tokens, further increasing modeling cost. Previous works ([Hong et al., 2023a](#); [Chen et al., 2024a](#)) compress point cloud features with Q-former, while others ([Fu et al., 2025](#); [Huang et al., 2025b](#)) adopt voxel-based representations to better preserve structure. However, these methods typically trade geometric fidelity for token efficiency, and the extracted point cloud features contain only limited semantic information, making

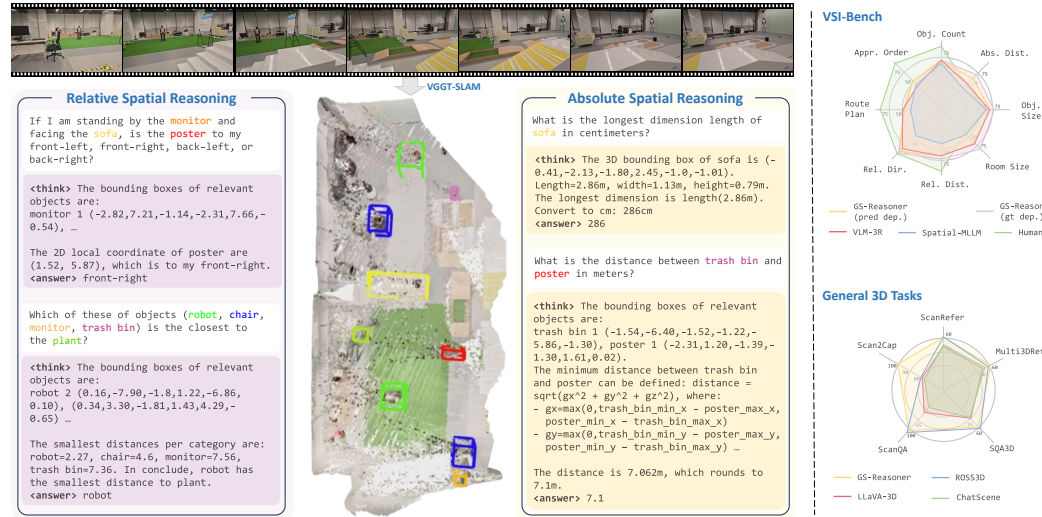


Figure 1: We propose *GS-Reasoner*, which integrates visual grounding as an intermediate chain-of-thought for spatial reasoning. All the bounding boxes shown above are autoregressively derived by *GS-Reasoner* in the reasoning process. Notably, the showcased video is captured in the wild without sensory 3D inputs, highlighting the strong generalization capability of our model.

accurate grounding and reasoning difficult. More recent approaches (Zheng et al., 2025; Zhu et al., 2024b) encode 3D positional cues into video-based semantic features from vision foundation models, showing promising 3D reasoning benefits from visual LLM pretraining. Nevertheless, the geometric cues derived solely from 3D position encodings are weak, which constrains grounding performance. The second challenge lies in the lack of high-quality datasets that integrate grounding as an intermediate step for spatial reasoning. Existing 3D VQA datasets (Azuma et al., 2022; Ma et al., 2022) provide only short answers without grounding annotations or reasoning steps, making the combination of grounding and reasoning impossible. Additionally, these datasets fail to capture the contextual richness and structural complexity required for comprehensive spatial reasoning, further limiting progress toward robust 3D LLMs.

In this work, we propose a novel approach to address the identified challenges by introducing a comprehensive 3D scene representation and a GCoT dataset for spatial reasoning. Our 3D scene representation integrates semantic features from vision foundation models, geometric features encoded by a point cloud encoder, and 3D positional information. The key idea is to unify these heterogeneous signals within an image patch-based representation. Specifically, we pool the geometric features of point maps in a dual-path way to align them with the corresponding semantic feature and 3D position of the image patch, and subsequently fuse them into a unified hybrid representation. This hybrid representation preserves the strong generalization ability of LLMs gained from visual-semantic pretraining, while the incorporation of geometric information significantly strengthens its 3D scene comprehension. As a result, *GS-Reasoner* can accurately locate objects without relying on any external modules, which provides a natural intermediate step for spatial reasoning. To train models capable of handling both tasks, we construct the GCoT dataset. It includes precise 3D bbox annotations for objects mentioned in reasoning questions, along with step-by-step reasoning paths that embed grounding as a core component of problem solving. By structuring the tasks in this way, the dataset encourages models to first identify relevant objects before addressing complex spatial reasoning, yielding a more interpretable and cognitively aligned approach to learning spatial reasoning.

- We propose a semantic-geometric hybrid 3D scene representation that endows LLM with strong geometric priors, firstly enabling LLM to autoregressively perform 3D visual grounding with impressive results.
- We introduce the GCoT dataset, which bridges the gap between grounding and spatial reasoning, enabling *GS-Reasoner* to first ground objects and then reason about their spatial relationships in a manner aligned with human cognition.
- We demonstrate the effectiveness of *GS-Reasoner* through extensive experiments, showcasing its remarkable performance in both 3D visual grounding and spatial reasoning tasks.

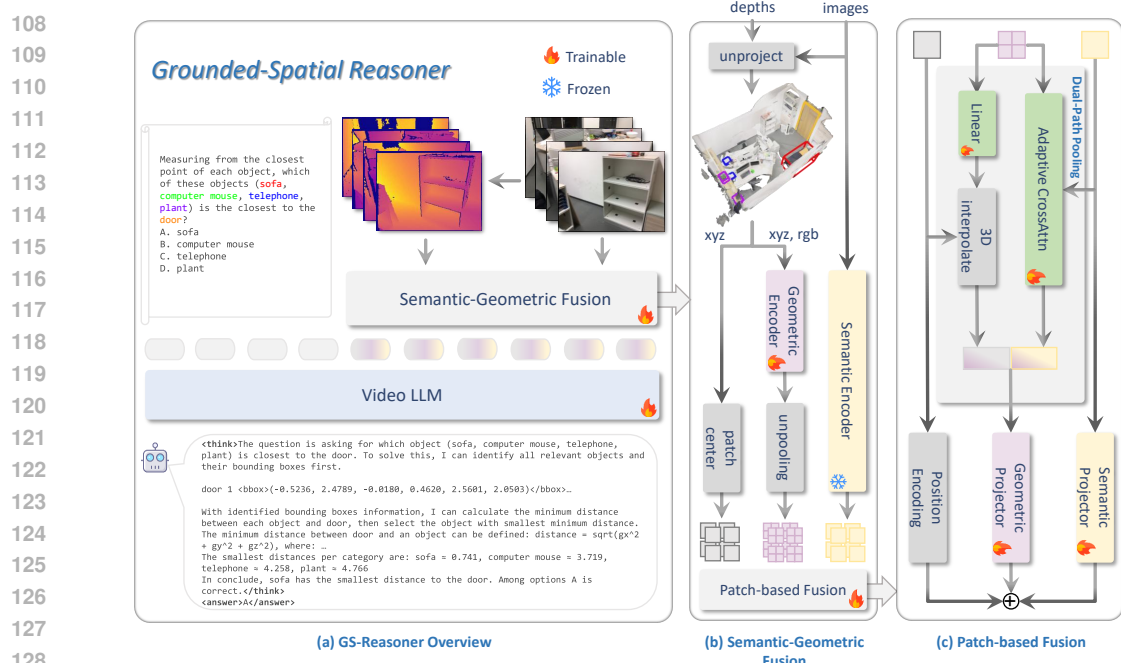


Figure 2: **Overview of GS-Reasoner framework.** Our method builds a semantic-geometric hybrid 3D scene representation, enabling 3D LLM to perform 3D visual grounding autoregressively, which allows grounding to be integrated as a chain-of-thought within the spatial reasoning process.

## 2 RELATED WORK

**3D Large Language Models for 3D Understanding.** Recent advances in MLLMs have enabled 3D LLMs that integrate 3D information for tasks such as 3D VQA, visual grounding, and captioning. Early work 3D-LLM (Hong et al., 2023a) introduces a Q-Former to align point cloud features with LLMs, followed by studies (Chen et al., 2024a;b; Zhu et al., 2024a; Deng et al., 2025) constructing 3D representations with controllable token lengths. Voxel-based approaches (Fu et al., 2025; Huang et al., 2025b) balance token efficiency and geometric fidelity, while object-centric methods (Huang et al., 2024; 2025b; Yu et al., 2025) improve 3D scene understanding but lack global context. Recent works (Zheng et al., 2025; Zhu et al., 2024b; Wang et al., 2025b) propose encoding 3D positional information into visual features extracted by vision foundation models, achieving promising results on 3D tasks while maintaining the generalization ability of visual LLMs. Despite these advances, existing 3D LLMs still struggle to jointly capture semantic and geometric information from 3D scenes, limiting performance on 3D visual grounding or forcing reliance on external modules.

**Video-Language Models for Spatial Reasoning.** The goal of visual-based spatial intelligence is to equip video MLLMs with the ability to understand and reason about 3D spatial structures directly from video data. While Video-Language Models (VLMs) (Lin et al., 2023; Li et al., 2024; Bai et al., 2025; Liu et al., 2024; Chen et al., 2024c) perform well on video-language tasks, they still show limited results on recent spatial reasoning benchmarks (Yang et al., 2025). Spatial-MLLM (Wu et al., 2025a) and VLM-3R (Fan et al., 2025) enhance spatial reasoning by incorporating geometric features from recent developed visual geometry models (e.g., VGGT (Wang et al., 2025c)) and constructing large-scale spatial reasoning QA pairs for training. However, the constrained answer formats, such as single-choice selections or short numerical responses, potentially limit the ability of MLLMs to fully exploit the rich 3D information encoded in the geometric features of visual geometry models.

## 3 GS-REASONER FRAMEWORK

### 3.1 OVERVIEW

Given a sequence of  $N$  RGB images  $\{I_i \in \mathbb{R}^{3 \times H \times W}\}_{i=1}^N$  of a 3D scene and a spatial reasoning query  $Q$ , our goal is to build a model that can first identify all objects potentially relevant to  $Q$  and

162 then perform step-by-step spatial reasoning in an autoregressive manner to derive the final answer.  
 163 Depth maps  $\{D_i \in \mathbb{R}^{H \times W}\}_{i=1}^N$ , camera intrinsics  $K \in \mathbb{R}^{3 \times 3}$ , and extrinsics  $\{T_i \in \mathbb{R}^{4 \times 4}\}_{i=1}^N$  are  
 164 assumed available or can be estimated using visual geometry methods (Maggio et al., 2025).

165 As illustrated in Fig. 2 (a) and (b), the proposed GS-Reasoner framework comprises three main  
 166 components: a semantic encoder, a geometric encoder, and a video LLM. The semantic encoder  
 167 extracts rich semantic features from the input RGB images using a pre-trained vision foundation  
 168 model. Meanwhile, the depth maps are back-projected into point maps  $\{P_i \in \mathbb{R}^{3 \times H \times W}\}_{i=1}^N$ , which  
 169 are subsequently transformed into geometric and 3D positional features. Specifically, the geometric  
 170 encoder processes the aggregated sensor point cloud  $\mathcal{P} = \bigcup_{i=1}^N P_i$ , where  $\mathcal{P} \in \mathbb{R}^{M \times 3}$  denotes  $M$  3D  
 171 points, to capture structural information of the scene. Since the geometric features are permutation-  
 172 invariant and thus lack explicit positional cues, we further position-encode the 3D coordinates of  
 173 points. Finally, the semantic, geometric, and positional features are fused into a unified semantic-  
 174 geometric hybrid 3D scene representation. This hybrid representation, together with the text query  
 175  $Q$ , is fed into the video LLM to perform autoregressive object grounding and spatial reasoning,  
 176 ultimately producing the final answer.

177 We format the output of GS-Reasoner in a Chain-of-Thought (CoT) manner. All intermediate reasoning  
 178 is enclosed within the "`<think>...</think>`" block: the model first analyzes the query,  
 179 and then lists the 3D bounding boxes of all relevant objects in the following format "`OBJECT_NAME`  
 180 `OBJECT_COUNT` `<bbox>(x1, y1, z1, x2, y2, z2)</bbox>...`". If object bounding  
 181 boxes are considered unhelpful for answering during question analysis, they are omitted. Each  
 182 tuple "`(x1, y1, z1, x2, y2, z2)`" denotes the coordinates of two opposite corners of an  
 183 axis-aligned 3D bounding box expressed in the world coordinate frame (units: meters). After grounding,  
 184 the model carries out step-by-step spatial reasoning using all available information. Finally,  
 185 it emits a concise final answer enclosed in "`<answer>...</answer>`". This autoregressive  
 186 output format improves interpretability while remaining flexible, enabling GS-Reasoner to be applied  
 187 to various 3D visual grounding and spatial-reasoning tasks without changing the architecture.

### 188 3.2 SEMANTIC-GEOMETRIC HYBRID 3D SCENE REPRESENTATION

190 In this section, we describe the construction of a comprehensive 3D scene representation that  
 191 seamlessly integrates semantic and geometric information. Building on Video LLM, our goal is  
 192 to enhance its spatial understanding capabilities by incorporating richer geometric cues, without  
 193 increasing the input token count or compromising its language comprehension. Inspired by recent  
 194 works (Zheng et al., 2025; Zhu et al., 2024b) that augment image patch features with 3D positional  
 195 encoding, we design our 3D scene representation using image patches as the basic building block.

196 **Geometric Feature Extraction.** The first challenge arises when extracting per-patch geometric  
 197 features from point maps. Instead of processing points independently within each patch—which often  
 198 contain very few points and thus provide limited context for effective feature learning—we process  
 199 the point cloud  $\mathcal{P}$  as a whole. Specifically, we first partition the point maps  $\{P_i \in \mathbb{R}^{3 \times H \times W}\}_{i=1}^N$   
 200 into patches of size  $p \times p$ , aligning with the image patch size used in the semantic encoder. To reduce  
 201 computational cost, we uniformly sample  $K$  points from each patch, resulting in subsampled point  
 202 maps denoted as  $\{P_i^{sub} \in \mathbb{R}^{3 \times K \times H' \times W'}\}_{i=1}^N$ , where  $H' = \frac{H}{p}$  and  $W' = \frac{W}{p}$ . The collection of all  
 203 sampled points across patches forms the input point cloud  $\mathcal{P}$ , which is subsequently processed by a  
 204 point cloud encoder to extract geometric features. We adopt the encoder-only Point Transformer v3  
 205 (PTv3) (Wu et al., 2024; 2025b) as our point cloud encoder owing to its efficiency and effectiveness.  
 206 Given a point set  $\mathcal{M} = (\mathcal{P}, \mathcal{F})$ , where  $\mathcal{F} \in \mathbb{R}^c$  denotes point attributes (e.g., position, color), PTv3  
 207 first serializes the input point cloud with space-filling curves and partitions the points into subsets  
 208  $[\mathcal{M}_1, \mathcal{M}_2, \dots, \mathcal{M}_{n'}]$  according to their serialization order. The serialized subsets are then processed  
 209 by a U-Net-like encoder-only architecture, where each layer employs serialized attention to capture  
 210 both local and global context. Between layers, each subset  $\mathcal{M}_i = (\mathcal{P}_i, \mathcal{F}_i)$  is pooled as follows,

$$211 \quad \mathbf{f}'_i = \text{MaxPool}(\{\mathbf{f}_j \mathbf{U} \mid \mathbf{f}_j \in \mathcal{F}_i\}), \quad \mathbf{p}'_i = \text{MeanPool}(\{\mathbf{p}_j \mid \mathbf{p}_j \in \mathcal{P}_i\}), \quad (1)$$

212 where  $(\mathbf{p}'_i, \mathbf{f}'_i)$  denotes the position and features of pooled point aggregated from subset  $\mathcal{M}_i$ , and  
 213  $\mathbf{U} \in \mathbb{R}^{c \times c'}$  is a linear projection. Collecting pooled points from  $n'$  subsets yields the point set  
 214  $\mathcal{M}' = \{\mathbf{p}'_i, \mathbf{f}'_i\}_{i=1}^{n'}$  for the next stage of encoding. Unpooling is performed by preserving mapping  
 215 relationships through the pooling layers, which allows point features to be projected back to the

216 original resolution and concatenated with features from the previous encoding stage as,  
 217

$$218 \quad \mathbf{f}_i^{up} = \text{concat}(\mathbf{f}_i, \mathbf{f}_j^{up}), \quad \text{if } (\mathbf{p}_i, \mathbf{f}_i) \in \mathcal{M}_j. \quad (2)$$

219 By progressively unpooling across layers and mapping the features back to point maps, we obtain the  
 220 final geometric feature maps  $\{G_i \in \mathbb{R}^{C \times K \times H' \times W'}\}_{i=1}^N$ , which are spatially aligned with the inputs.  
 221

222 **Dual-Path Pooling.** With extracted geometric feature maps  $\{G_i \in \mathbb{R}^{C \times K \times H' \times W'}\}_{i=1}^N$  and point  
 223 maps  $\{P_i^{sub} \in \mathbb{R}^{3 \times K \times H' \times W'}\}_{i=1}^N$ , a straightforward strategy for deriving per-patch representations  
 224 is to apply max pooling within each patch on the geometric feature maps and mean pooling on the  
 225 point maps, following the design in PTv3. However, we observed that this naive approach results in  
 226 poor grounding performance, which can be attributed to two key issues: **(1) semantic-geometric  
 227 misalignment.** While processing point cloud as a whole enhances the receptive field and enables more  
 228 accurate geometric feature extraction compared to treating points within each patch independently, it  
 229 also leads to misalignment between the geometric features and semantic features in each patch, as  
 230 the 3D points in a patch can interact with almost all the points in point cloud, whereas the semantic  
 231 features are constrained to the information visible in the current image. The geometric features pooled  
 232 by max pooling emphasize the most salient features without considering the semantic context of  
 233 the patch, exacerbating this misalignment. **(2) position-geometric misalignment.** Traditional point  
 234 cloud encoders typically group points using KNN (Qi et al., 2017a;b; Zhao et al., 2021; Wu et al.,  
 235 2022) or serialization (Wu et al., 2024; 2025b), ensuring that points within a group are spatially close  
 236 in 3D space. This spatial proximity allows naive pooling strategies to effectively preserve geometric  
 237 information within the group. In contrast, 3D points within an image patch do not necessarily satisfy  
 238 this condition, particularly when a patch contains both foreground and background elements, which  
 239 can lead to large spatial distances among points. Consequently, directly applying max pooling to the  
 240 geometric features within the patch may introduce geometric inconsistencies, while mean pooling the  
 241 3D points can produce positions that are far from both foreground and background objects. These  
 242 issues can negatively impact the accuracy of predicted 3D bounding boxes.  
 243

244 To address these challenges, we propose a simple yet effective dual-path feature fusion module that  
 245 aligns semantic, geometric, and positional information at the patch level. To mitigate semantic-  
 246 geometric misalignment, we construct semantic-aligned geometric features via a lightweight cross-  
 247 attention network. Each patch’s semantic feature serves as the query, while the  $K$  geometric features  
 248 within the patch serve as keys and values. The attention mechanism allows the network to selectively  
 249 integrate the geometric features most relevant to the patch’s semantic context. For the position-  
 250 geometric misalignment, we directly sample the 3D point corresponding to each patch’s center pixel  
 251 for position encoding, and then interpolate the geometric features based on the position of the 3D  
 252 point to obtain position-aligned geometric feature. This simple strategy ensures consistency between  
 253 positional and geometric information: if the sampled point is on the foreground, the interpolated  
 254 features mainly come from foreground points, and vice versa. Finally, the semantic-aligned and  
 255 position-aligned geometric features are concatenated and projected to produce the final patch-level  
 256 geometric features, which are then combined with the projected semantic feature and sampled 3D  
 257 point positional encoding to obtain the final patch-level hybrid feature.  
 258

## 259 4 GCoT: GROUNDED CHAIN-OF-THOUGHT DATASET

260 Recent works (Wu et al., 2025a; Fan et al., 2025; Ouyang et al., 2025) attempt to improve the  
 261 spatial reasoning ability of MLLMs by constructing large-scale QA pairs with 3D object annotations.  
 262 However, the answers in these datasets are typically restricted to single choices or short numerical  
 263 values. Such limited supervision narrows the learning space of MLLMs, thereby reducing their  
 264 learning efficiency and resulting in less interpretable outcomes. In fact, spatial reasoning is largely  
 265 grounded in the locations and size relationships of relevant objects, indicating that identifying objects  
 266 and reasoning about their geometry are fundamental steps, which is essentially a 3D visual grounding  
 267 task. Introducing grounding as an intermediate step in spatial reasoning not only provides richer  
 268 supervision but also improves interpretability, which motivates the construction of the GCoT dataset.  
 269

270 Fig. 3 presents an overview of the GCoT dataset. We first generate spatial reasoning QA pairs without  
 271 CoT by following the dataset construction pipeline of (Yang et al., 2025; Fan et al., 2025), while  
 272 preserving the object bounding box information used during generation. Leveraging the QA pairs,  
 273 object bounding boxes, and bird’s-eye views of the scenes, we then prompt GPT-4o (OpenAI et al.,  
 274

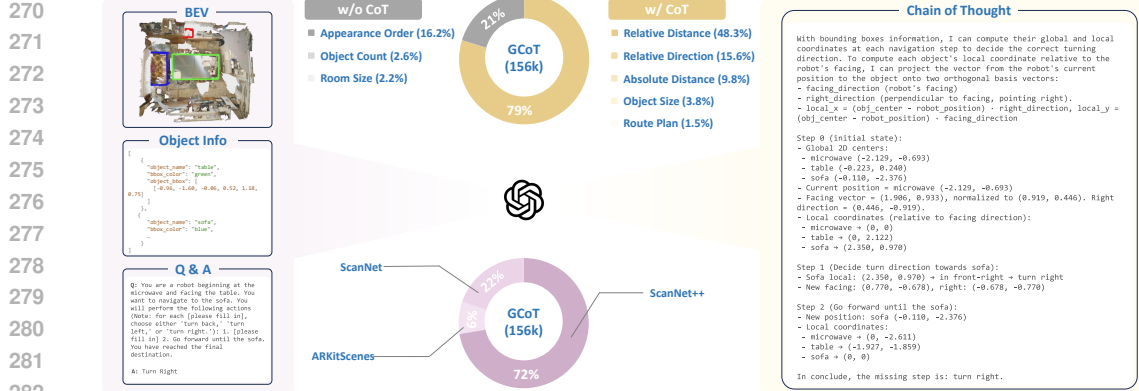


Figure 3: **Overview of Grounded Chain-of-Thought (GCoT) Dataset.** We first construct spatial QA pairs without CoT, and then prompt GPT-4o to generate CoT paths based on the bird’s-eye view, object information, and QA pairs.

2024) to produce coherent CoT reasoning paths that lead to the final answers. The resulting dataset consists of 156k QA pairs, among which 79% contain CoT annotations. We omit CoT construction for the Appearance Order, Object Counting, and Room Size Estimation tasks, as these tasks do not require complex spatial reasoning. Additional details are provided in the Appendix A.

## 5 EXPERIMENTS

We first describe the implementation details in Section 5.1 and report results on 3D visual grounding in Section 5.2. Since grounding forms the basis for spatial reasoning, we then evaluate our framework on spatial reasoning tasks in Section 5.3. Section 5.4 presents additional results on general 3D tasks, and Section 5.5 provides zero-shot evaluation and ablation studies to analyze the contributions of individual model components and the proposed GCoT dataset.

### 5.1 IMPLEMENTATION DETAILS

**Model Architecture.** GS-Reasoner is developed on top of LLaVA-Video 7B (Zhang et al., 2024), an open-source video LLM based on Qwen2-7B (Team, 2024). For semantic encoding, we adopt SigLIP (Zhai et al., 2023), a vision transformer pre-trained on large-scale image–text pairs through contrastive learning. For geometric encoding, we employ Sonata (Wu et al., 2025b), an efficient point cloud encoder built upon PTv3 (Wu et al., 2024) and pre-trained in a self-supervised manner on large-scale point cloud datasets. We adopt sinusoidal positional encoding (Vaswani et al., 2017) to encode the 3D positions of image patches.

**Training.** GS-Reasoner is trained end-to-end for next-token prediction. We first pretrain on subsets of 3D visual grounding datasets, including ScanRefer (Chen et al., 2020), Multi3DRef (Zhang et al., 2023), SR3D, and NR3D (Achlioptas et al., 2020), to warm up object grounding, and then finetune on our proposed GCoT dataset, the remaining grounding data, and other 3D tasks (ScanQA (Azuma et al., 2022), SQA3D (Ma et al., 2022), Scan2Cap (Chen et al., 2021)). Data augmentation is important for training GS-Reasoner and we provide more details in Appendix B.1.

**Inference.** Unless otherwise specified, we uniformly sample 32 images from each scene as the model input during inference. For the 3D visual grounding task, ground-truth depth maps and camera parameters are provided to ensure a fair evaluation. For the spatial reasoning task, depth maps and camera parameters are estimated using VGGT-SLAM (Maggio et al., 2025), followed by metric alignment with Moge2 (Wang et al., 2025e). More details are provided in Appendix B.2.

### 5.2 EVALUATION ON 3D VISUAL GROUNDING

We evaluate our model on four widely used 3D visual grounding benchmarks: ScanRefer, Multi3DRef, SR3D, and NR3D. For single-object grounding (ScanRefer, SR3D, NR3D), we report Acc@25 and

324 **Table 1: Evaluation on 3D Visual Grounding.** GS-Reasoner achieves performance comparable to 3D LLMs  
325 using mesh proposals or external grounding, without any external components.

326 <b>Methods</b>	327 ScanRefer		328 Multi3DRef		329 SR3D	330 NR3D
	331 Acc@25	332 Acc@50	333 F1@25	334 F1@50	335 Acc@25	336 Acc@25
<i>328 Expert Models</i>						
329 3D-VisTA (Zhu et al., 2023)	51.0	46.2	-	-	56.5	47.7
330 PQ3D (Zhu et al., 2024c)	56.7	51.8	-	-	62.0	52.2
331 UniVLG (Jain et al., 2025)	63.5	56.4	-	-	73.0	56.3
332 Locate 3D (McVay et al., 2025)	61.1	50.9	-	-	68.2	56.1
<i>3D LLMs + Proposals from Mesh PC</i>						
333 Chat-Scene (Huang et al., 2024)	55.5	50.2	57.1	52.4	-	-
334 Inst3D-LMM (Yu et al., 2025)	57.8	51.6	58.3	53.5	-	-
335 Video-3D LLM (Zheng et al., 2025)	58.1	51.7	58.0	52.7	-	-
336 ROSS3D (Wang et al., 2025b)	61.1	54.4	59.6	54.3	-	-
337 SeeGround (Li et al., 2025b)	44.1	39.4	-	-	-	-
<i>3D LLMs + External Grounding Module</i>						
338 Grounded 3D-LLM (Chen et al., 2024b)	48.6	44.0	44.7	40.8	-	-
339 ReGround3D (Zhu et al., 2024a)	53.1	41.2	-	-	-	-
340 LLaVA-3D (Zhu et al., 2024b)	54.1	42.2	54.3	47.2	-	-
<i>3D LLMs</i>						
341 3D-LLM (Hong et al., 2023b)	30.3	-	-	-	-	-
<b>GS-Reasoner</b>	<b>60.8</b>	<b>42.2</b>	<b>61.7</b>	<b>45.3</b>	<b>56.7</b>	<b>50.0</b>

342 **Table 2: Evaluation on VSI-Bench.** GS-Reasoner achieves state-of-the-art performance on most  
343 tasks, with further gains using more accurate (ground-truth) depth.

345 <b>Methods</b>	346 Rank.	347 Avg.	348 Numerical Question				349 Multiple-Choice Question			
			350 Obj.	351 Cnt.	352 Abs. Dist.	353 Obj. Size	354 Room Size	355 Rel. Dist.	356 Rel. Dir.	357 Route Plan
<i>359 Baseline</i>										
360 Chance Level (Random)	-	-	-	-	-	-	25.0	36.1	28.3	25.0
361 Chance Level (Frequency)	-	34.0	62.1	32.0	29.9	33.1	25.1	47.9	28.4	25.2
<i>362 VSI-Bench Perf. (<math>\dagger</math>=Tiny Set)</i>										
363 $\dagger$ Human Level	-	79.2	94.3	47.0	60.4	45.9	94.7	95.8	95.8	100.0
364 $\dagger$ Gemini-1.5 Flash	-	45.7	50.8	33.6	56.5	45.2	48.0	39.8	32.7	59.2
365 $\dagger$ Gemini-1.5 Pro	-	48.8	49.6	28.8	58.6	49.4	46.0	48.1	42.0	68.0
366 $\dagger$ Gemini-2.0 Flash	-	45.4	52.4	30.6	66.7	31.8	56.0	46.3	24.5	55.1
<i>367 Proprietary Models (API)</i>										
368 GPT-4o	3	34.0	46.2	5.3	43.8	38.2	37.0	41.3	31.5	28.5
369 Gemini-1.5 Flash	2	42.1	49.8	30.8	53.5	54.4	37.7	41.0	31.5	37.8
370 Gemini-1.5 Pro	1	45.4	56.2	30.9	64.1	43.6	51.3	46.3	36.0	34.6
<i>371 Open-sourced VLMS</i>										
372 InternVLL2-40B	3	36.0	34.9	26.9	46.5	31.8	42.1	32.2	34.0	39.6
373 LongVILA-8B	9	21.6	29.1	9.1	16.7	0.0	29.6	30.7	32.5	25.5
374 VILA-1.5-40B	7	31.2	22.4	24.8	48.7	22.7	40.5	25.7	31.5	32.9
375 LongVA-7B	8	29.2	38.0	16.6	38.9	22.2	33.1	43.3	25.4	15.7
376 LLaVA-NeXT-Video-7B	4	35.6	48.5	14.0	47.8	24.2	43.5	42.4	34.0	30.6
377 LLaVA-NeXT-Video-72B	1	40.9	48.9	22.8	57.4	35.3	42.4	36.7	35.0	48.6
378 QWen2.5VL-7B	5	33.0	40.9	14.8	43.4	10.7	38.6	38.5	33.0	29.8
379 LLaVA-OneVision-7B	6	32.4	47.7	20.2	47.4	12.3	42.5	35.2	29.4	24.4
380 LLaVA-OneVision-72B	2	40.2	43.5	23.9	57.6	37.5	42.5	39.9	32.5	44.6
<i>381 Specialized Spatial Reasoning Models</i>										
382 Spatial-MLLM-4B	3	48.4	65.3	34.8	63.1	45.1	41.3	46.2	33.5	46.3
383 VLM-3R-7B	2	60.9	70.2	49.4	69.2	67.1	65.4	80.5	45.4	40.1
<b>384 GS-Reasoner (pred dep.)</b>	<b>1</b>	<b>64.7</b>	<b>69.1</b>	<b>61.9</b>	<b>70.0</b>	<b>65.7</b>	<b>65.4</b>	<b>88.9</b>	<b>44.3</b>	<b>52.3</b>
<b>385 GS-Reasoner (gt dep.)</b>	-	70.1	70.9	73.6	77.8	81.8	70.6	90.5	42.8	52.6

386 Acc@50, where a prediction is correct if its Intersection over Union (IoU) with ground truth exceeds  
387 0.25 or 0.5, respectively. For multi-object grounding (Multi3DRef), we use the F1 score computed  
388 at IoU thresholds of 0.25 and 0.5. For fair comparison, we group the baselines into four categories:  
389 (1) Expert Models, specifically designed for 3D grounding and trained with both bounding box and  
390 mask supervision; (2) 3D LLMs + Proposals from Mesh Point Cloud, which select from proposals  
391 generated by detectors such as Mask3D (Schult et al., 2022); (3) 3D LLMs + External Grounding  
392 Module, which pair a 3D LLM with an auxiliary grounding module; and (4) 3D LLMs, which directly  
393 predict bounding boxes autoregressively without relying on any external modules or proposals.

394 As shown in Tab. 1, our model achieves superior performance compared with 3D-LLM (Hong et al.,  
395 2023b). Among other 3D LLM-based methods, it achieves state-of-the-art F1@25 on Multi3DRef,  
396 even surpassing methods that rely on proposals or external grounding modules. Moreover, on

378 **Table 3: Evaluation on General 3D Tasks.** GS-Reasoner outperforms state-of-the-art 3D LLMs on Scan2Cap  
 379 and achieves comparable results on ScanQA and SQA3D.

380 381 382 383 384 385 386 387 388 389 390 391 392 393 394 395 396 397 398 399 400 401 402 403 404 405 406 407 408 409 410 411 412 413 414 415 416 417 418 419 420 421 422 423 424 425 426 427 428 429 430 431	Scan2Cap				ScanQA				SQA3D	
	B-4 ↑	Rouge ↑	CIDEr ↑	Meteor ↑	B-4 ↑	Rouge ↑	CIDEr ↑	Meteor ↑	EM ↑	EM ↑
3D-LLM(flamingo) (Hong et al., 2023a)	-	-	-	-	7.2	32.3	59.2	12.2	20.4	-
3D-LLM(BLIP2-flant5) (Hong et al., 2023a)	-	-	-	-	12.0	35.7	69.4	14.5	20.5	-
LL3DA (Chen et al., 2024a)	36.8	55.1	65.2	26.0	13.5	37.3	76.8	15.9	-	-
Chat-3Dv2 (Huang et al., 2023a)	-	-	-	-	14.0	-	87.6	-	-	54.7
LEO (Huang et al., 2023b)	36.9	57.8	68.4	27.7	13.2	49.2	101.4	20.0	24.5	50.0
Scene-LLM (Fu et al., 2025)	-	-	-	-	12.0	40.0	80.0	16.6	27.2	54.2
ChatScene (Huang et al., 2024)	36.3	58.1	77.2	28.0	14.3	41.6	87.7	18.0	21.6	54.6
LLA-VA-3D (Zhu et al., 2024b)	41.1	63.4	79.2	30.2	14.5	50.1	91.7	20.7	27.0	55.6
Video-3D LLM (Zheng et al., 2025)	42.4	62.3	83.8	28.9	16.2	49.0	102.1	19.8	30.1	58.6
ROSS3D (Wang et al., 2025b)	43.4	66.9	81.3	30.3	17.9	50.7	107.0	20.9	30.8	63.0
<b>GS-Reasoner</b>	<b>47.6</b>	<b>69.2</b>	<b>101.0</b>	<b>32.1</b>	<b>16.2</b>	<b>49.2</b>	<b>102.6</b>	<b>19.8</b>	<b>29.9</b>	<b>59.9</b>

ScanRefer Acc@50 and Multi3DRef F1@50, GS-Reasoner matches the performance of 3D LLMs with external grounding modules, despite using only noisy, incomplete sensor point clouds rather than high-quality mesh inputs. However, GS-Reasoner still lags behind 3D LLMs with proposals from mesh point clouds on these two metrics. We attribute this to two factors: (1) mesh point clouds are more complete and less noisy; and (2) conventional 3D detectors (e.g., Mask3D) are commonly trained with mask supervision, which is more conducive to precise object localization than bbox supervision, as also reported in (McVay et al., 2025; Jain et al., 2025). An interesting observation is that GS-Reasoner achieves comparable results to expert models on ScanRefer but falls behind on SR3D and NR3D, suggesting LLM-based methods are better at complex queries (as in ScanRefer), while expert models excel in precise localization for simpler descriptions (as in SR3D and NR3D).

### 5.3 EVALUATION ON SPATIAL REASONING

We evaluate GS-Reasoner’s spatial reasoning capability on VSI-Bench (Yang et al., 2025), which comprises over 5,000 QA pairs from egocentric videos in ScanNet (Dai et al., 2017), ScanNet++ (Yeshwanth et al., 2023), and ARKitScenes (Baruch et al., 2021). VSI-Bench provides two answer formats, multiple choice (MCA) and numerical (NA), and covers eight tasks spanning spatial and temporal reasoning. We follow the official VSI-Bench evaluation protocol for metric computation. The results in Tab. 2 demonstrate that GS-Reasoner achieves impressive performance, particularly on the Relative Direction and Absolute Distance tasks, which require complex spatial reasoning and precise 3D object localization. It also attains state-of-the-art results on the Appearance Order task, indicating that our semantic-geometric hybrid features effectively preserve temporal information from the original video while providing additional spatial cues. Moreover, performance consistently improves with more accurate depth input, with the average score exceeding 70 and yielding nearly a 10-point gain over the previous state of the art.

### 5.4 EVALUATION ON GENERAL 3D TASKS

We further present results on three established 3D vision-language understanding tasks: Scan2Cap, ScanQA, and SQA3D, following the official protocols and reporting performance in terms of CIDEr, BLEU, METEOR, ROUGE, and exact-match (EM) accuracy. The results in Tab. 3 show that GS-Reasoner sets a new state of the art for 3D dense captioning, achieving the best results on Scan2Cap across all metrics and significantly surpassing the previous leading method, ROSS3D (Wang et al., 2025b). We attribute these gains to explicitly predicting coordinates for 3D visual grounding, which forces the model to better capture geometric and positional cues, thereby improving dense captioning performance. However, GS-Reasoner does not achieve leading results on ScanQA and SQA3D. We believe the main reasons are the presence of many ambiguous questions in these datasets that do not clearly specify the target object, as well as a strong bias in answer distribution. These factors encourage the model to overfit to textual patterns instead of effectively exploiting 3D tokens. Recent studies (Huang et al., 2025a; Li et al., 2025a) have also shown that finetuning LLMs without 3D input can yield results comparable to the state of the art on ScanQA and SQA3D. Incorporating reconstruction constraints in the output (as done in ROSS3D (Wang et al., 2025b)) may help encourage the model to utilize 3D tokens, and we leave this for future research.

432 5.5 ANALYSIS AND ABLATION STUDIES  
433434 Table 4: **Zero-shot 3D visual grounding.** We train the models exclusively on ScanNet and evaluate them  
435 on ScanNet++ and ARKitScenes for visual grounding, reporting all results in Acc@25. Note that GPT-4o is  
436 prompted to do 2D visual grounding and then back-project to 3D via depth map. Locate 3D is an expert model.  
437

Methods	ScanRefer	LX3D	
	ScanNet	ScanNet++	ARKitScenes
GPT-4o VLM	59.9	60.5	26.8
Locate 3D	61.1	56.7	46.2
<b>GS-Reasoner</b>	60.8	51.0	45.6

443 Table 5: **Ablation Study on Data Aug. and 3D Representation.** We train models to autoregressively predict  
444 3D bounding box coordinates using ScanRefer and Multi3DRef, and report results on ScanRefer.  
445

Methods	Data Aug.	Pos. Enc.	Geo.Pool.	Acc@25	Acc@50
LLaVA-NeXT	✗	✗	✗	0.0	0.0
Video-3D LLM	✗	Avg	✗	15.4	3.5
	✓	Avg	✗	53.2	29.8
	✓	Avg	Max	57.5 <sub>+4.3</sub>	35.7 <sub>+5.9</sub>
	✓	Avg	Cross-Attn	58.9 <sub>+5.7</sub>	38.6 <sub>+9.8</sub>
	✓	Sample	Interpolate	59.3 <sub>+6.1</sub>	40.2 <sub>+10.4</sub>
<b>GS-Reasoner</b>	✓	Sample	Dual-Path	<b>60.8<sub>+7.6</sub></b>	<b>42.2<sub>+12.4</sub></b>

453 Table 6: **Ablation Study on Grounded CoT Mechanism.** We report results only for tasks in the GCoT dataset  
454 that include CoT annotations, to highlight the effectiveness of grounded CoT.  
455

Methods	Avg.	Numerical Question		Multiple-Choice Question		
		Abs. Dist.	Obj. Size	Rel. Dist.	Rel. Dir.	Route Plan
LLaVA-NeXT-Video ft (w/o CoT)	52.3	45.1	64.3	58.9	60.7	32.5
GS-Reasoner ft (w/o CoT)	57.7 <sub>+5.4</sub>	50.8 <sub>+5.7</sub>	65.7 <sub>+1.4</sub>	62.3 <sub>+3.4</sub>	79.3 <sub>+18.6</sub>	30.4 <sub>-2.1</sub>
<b>GS-Reasoner ft (Full)</b>	<b>66.1<sub>+13.8</sub></b>	<b>61.9<sub>+16.8</sub></b>	<b>70.0<sub>+5.7</sub></b>	<b>65.4<sub>+6.5</sub></b>	<b>88.9<sub>+28.2</sub></b>	<b>44.3<sub>+11.8</sub></b>

460 **Zero-shot Generalization.** We evaluate the zero-shot generalization of GS-Reasoner on unseen  
461 3D scenes. The model is trained solely on ScanNet data (ScanRefer, SR3D, etc.), and tested on the  
462 ScanNet++ and ARKitScenes validation splits of the Locate3D dataset (McVay et al., 2025) without  
463 finetuning. As shown in Tab. 4, GS-Reasoner achieves performance comparable to SOTA expert  
464 models on ARKitScenes and demonstrates strong results in novel scene spatial reasoning (Fig. 1).  
465466 **Effectiveness of Data Augmentation and Semantic-Geometric Hybrid 3D Representation.** We  
467 conduct ablation studies to assess the effectiveness of our data augmentation strategies and the  
468 proposed semantic-geometric hybrid 3D representation, using the 3D visual grounding task as the  
469 evaluation benchmark. We believe this task directly reflects the model’s ability to jointly leverage  
470 semantic and spatial information from the input 3D scene. The results in Tab. 5 show that the model  
471 fails to accurately predict 3D bbox coordinates when only image input is provided (LLaVA-Next).  
472 Incorporating average position encoding (as in Video-3D LLM) still results in poor performance due  
473 to overfitting. Data augmentation brings notable improvements, yet the model continues to struggle  
474 with precise object localization, as indicated by the low Acc@50. Finally, by introducing geometric  
475 features from the geometric encoder and employing Dual-Path Pooling to progressively fuse position-  
476 aligned and semantic-aligned geometric features, we achieve substantial gains in both Acc@25 and  
477 Acc@50. These results demonstrate that the proposed hybrid 3D representation strengthens the  
478 model’s understanding of 3D scenes and enables more accurate visual grounding.479 **Effectiveness of GCoT Dataset.** We also ablate the impact of incorporating grounding into the  
480 chain-of-thought process on spatial reasoning performance. Specifically, we remove the CoT part  
481 from the answers in the GCoT dataset and train the model to directly predict the answer from  
482 the 3D scene and question. We report results for five tasks that incorporate grounding within the  
483 CoT process in Tab. 6. The results show that integrating grounding as part of the CoT process  
484 substantially improves performance across all tasks, particularly in object absolute distance, object  
485 relative direction, and route planning. This highlights the importance of not only providing the model  
486 with grounding capabilities but also guiding it to leverage grounding effectively to support spatial  
487 reasoning, demonstrating the necessity of the proposed GCoT dataset.

486  
487  
488  
489  
490  
491  
492  
493  
494  
495  
496  
497  
498  
499  
500  
501  
502  
503  
504  
505  
506  
507  
508  
509  
510  
511  
512  
513  
514  
515  
516  
517  
518  
519  
520  
521  
522  
523  
524  
525  
526  
527  
528  
529  
530  
531  
532  
533  
534  
535  
536  
537  
538  
539Table 7: **Computation Cost Comparison.** All values are reported in milliseconds.

Methods	2D Vision Enc.	3D Vision Enc.	Dual-Path	Total
LLaVA-NeXT-Video	429	-	-	470
<b>GS-Reasoner</b>	430	204	41	737

**Computation Costs Evaluation.** GS-Reasoner’s computational overhead compared to the backbone LLaVA-Next-Video primarily arises from the construction of visual tokens. Specifically, GS-Reasoner requires encoding point clouds using Point Transformer and integrating them into image patch features. Therefore, we conduct a comparison of computational overhead during the visual token construction phase, using a single 4090 GPU with 32 input images. As shown in Tab. 7, GS-Reasoner introduces some additional computational overhead. However, since all visual tokens only need to be constructed once per response, this overhead is acceptable relative to the overall inference time. Furthermore, during subsequent reasoning, the semantic-geometric hybrid 3D representation constructed by GS-Reasoner does not increase the number of visual tokens, so the inference time remains comparable to that of LLaVA-Next-Video.

Table 8: **Ablation Study on Input Frames.** We investigate the impact of different numbers of input frames and sampling strategies on 3D visual grounding performance.

Frames Num	Sampling Strategy	ScanRefer		Multi3DRef	
		Acc@25	Acc@50	F1@25	F1@50
32	uniform	60.8	42.2	61.7	45.3
48	uniform	<b>61.7</b>	44.5	62.2	46.9
64	uniform	61.2	<b>45.1</b>	<b>62.5</b>	<b>48.0</b>
32	cdviews	61.1	43.4	61.9	46.2

**Ablation Study on Input Frames.** We conduct an ablation study to investigate the impact of different numbers of input frames and sampling strategies on 3D visual grounding performance. As shown in Tab. 8, model performance consistently improves with an increasing number of input images, and the improvements are more pronounced in Acc@50 (F1@50) compared to Acc@25 (F1@25), indicating that providing denser point clouds can indeed help enhance localization accuracy. Moreover, employing context-aware sampling strategies such as cdViews (Wang et al., 2025a) also yields certain improvements.

## 6 CONCLUSION

In this work, we present GS-Reasoner, a novel framework that integrates grounding into spatial reasoning as a chain-of-thought process. Built upon a hybrid semantic-geometric 3D scene representation, GS-Reasoner performs grounding without requiring any external modules, making it a natural intermediate step for spatial reasoning. The GCoT dataset further strengthens the model’s ability to handle both tasks effectively.

540 ETHICS STATEMENT  
541

542 Our work introduces a new dataset generated entirely using large language models (LLMs). As  
543 the dataset is synthetically generated, it does not contain any personally identifiable information  
544 or sensitive human data. Nevertheless, synthetic data may inherit biases present in the underlying  
545 LLM, and could potentially be misused for harmful or misleading purposes. To mitigate these risks,  
546 the dataset is intended solely for academic research, and will be released with clear guidelines on  
547 responsible usage. Users are encouraged to consider ethical implications when employing the dataset  
548 for downstream tasks.

549  
550 REPRODUCIBILITY STATEMENT  
551

552 To facilitate reproducibility, we will release the full dataset, preprocessing scripts, and detailed  
553 documentation upon acceptance. All experimental code, pretrained models, and evaluation protocols  
554 will also be made publicly available. The datasets used in our experiments are either publicly  
555 accessible or will be released as part of this work. We provide complete hyperparameter settings,  
556 training schedules, and random seeds in the paper and supplementary materials.

557  
558 REFERENCES  
559

560 Panos Achlioptas, Ahmed Abdelreheem, Fei Xia, Mohamed Elhoseiny, and Leonidas Guibas.  
561 Referit3d: Neural listeners for fine-grained 3d object identification in real-world scenes. In  
562 *European conference on computer vision*, pp. 422–440. Springer, 2020. [6](#), [18](#)

563 Daichi Azuma, Taiki Miyanishi, Shuhei Kurita, and Motoaki Kawanabe. Scanqa: 3d question  
564 answering for spatial scene understanding. In *proceedings of the IEEE/CVF conference on*  
565 *computer vision and pattern recognition*, pp. 19129–19139, 2022. [2](#), [6](#), [18](#)

566 Shuai Bai, Keqin Chen, Xuejing Liu, Jialin Wang, Wenbin Ge, Sibo Song, Kai Dang, Peng Wang,  
567 Shijie Wang, Jun Tang, et al. Qwen2. 5-vl technical report. *arXiv preprint arXiv:2502.13923*, 2025.  
568 [3](#)

569 Gilad Baruch, Zhuoyuan Chen, Afshin Dehghan, Tal Dimry, Yuri Feigin, Peter Fu, Thomas Gebauer,  
570 Brandon Joffe, Daniel Kurz, Arik Schwartz, et al. Arkitscenes: A diverse real-world dataset for 3d  
571 indoor scene understanding using mobile rgb-d data. *arXiv preprint arXiv:2111.08897*, 2021. [8](#), [16](#)

573 Wenxiao Cai, Iaroslav Ponomarenko, Jianhao Yuan, Xiaoqi Li, Wankou Yang, Hao Dong, and  
574 Bo Zhao. Spatialbot: Precise spatial understanding with vision language models. *arXiv preprint*  
575 *arXiv:2406.13642*, 2024. [1](#)

576 Dave Zhenyu Chen, Angel X Chang, and Matthias Nießner. Scanrefer: 3d object localization in rgb-d  
577 scans using natural language. *16th European Conference on Computer Vision (ECCV)*, 2020. [6](#), [18](#)

578 Sijin Chen, Xin Chen, Chi Zhang, Mingsheng Li, Gang Yu, Hao Fei, Hongyuan Zhu, Jiayuan Fan, and  
579 Tao Chen. Ll3da: Visual interactive instruction tuning for omni-3d understanding reasoning and  
580 planning. In *Proceedings of the IEEE/CVF conference on computer vision and pattern recognition*,  
581 pp. 26428–26438, 2024a. [1](#), [3](#), [8](#)

583 Xingyu Chen, Yue Chen, Yuliang Xiu, Andreas Geiger, and Anpei Chen. Ttt3r: 3d reconstruction as  
584 test-time training. *arXiv preprint arXiv:2509.26645*, 2025. [19](#)

585 Yilun Chen, Shuai Yang, Haifeng Huang, Tai Wang, Runsen Xu, Ruiyuan Lyu, Dahua Lin, and  
586 Jiangmiao Pang. Grounded 3d-llm with referent tokens. *arXiv preprint arXiv:2405.10370*, 2024b.  
587 [3](#), [7](#)

588 Zhe Chen, Weiyun Wang, Yue Cao, Yangzhou Liu, Zhangwei Gao, Erfei Cui, Jinguo Zhu, Shenglong  
589 Ye, Hao Tian, Zhaoyang Liu, et al. Expanding performance boundaries of open-source multimodal  
590 models with model, data, and test-time scaling. *arXiv preprint arXiv:2412.05271*, 2024c. [3](#)

592 Zhenyu Chen, Ali Gholami, Matthias Nießner, and Angel X Chang. Scan2cap: Context-aware dense  
593 captioning in rgb-d scans. In *Proceedings of the IEEE/CVF conference on computer vision and*  
594 *pattern recognition*, pp. 3193–3203, 2021. [6](#), [18](#)

594 An-Chieh Cheng, Hongxu Yin, Yang Fu, Qiushan Guo, Ruihan Yang, Jan Kautz, Xiaolong Wang,  
 595 and Sifei Liu. Spatialrgpt: Grounded spatial reasoning in vision-language models. *Advances in*  
 596 *Neural Information Processing Systems*, 37:135062–135093, 2024. 1

597

598 Angela Dai, Angel X Chang, Manolis Savva, Maciej Halber, Thomas Funkhouser, and Matthias  
 599 Nießner. Scannet: Richly-annotated 3d reconstructions of indoor scenes. In *Proceedings of the*  
 600 *IEEE conference on computer vision and pattern recognition*, pp. 5828–5839, 2017. 8, 16

601

602 Jiajun Deng, Tianyu He, Li Jiang, Tianyu Wang, Feras Dayoub, and Ian Reid. 3d-llava: Towards  
 603 generalist 3d llms with omni superpoint transformer. In *Proceedings of the Computer Vision and*  
 604 *Pattern Recognition Conference*, pp. 3772–3782, 2025. 3

605

606 Runpei Dong, Zekun Qi, Linfeng Zhang, Junbo Zhang, Jianjian Sun, Zheng Ge, Li Yi, and Kaisheng  
 607 Ma. Autoencoders as cross-modal teachers: Can pretrained 2d image transformers help 3d  
 608 representation learning? *arXiv preprint arXiv:2212.08320*, 2022. 19

609

610 Zhiwen Fan, Jian Zhang, Renjie Li, Junge Zhang, Runjin Chen, Hezhen Hu, Kevin Wang, Huaizhi Qu,  
 611 Dilin Wang, Zhicheng Yan, Hongyu Xu, Justin Theiss, Tianlong Chen, Jiachen Li, Zhengzhong  
 612 Tu, Zhangyang Wang, and Rakesh Ranjan. Vlm-3r: Vision-language models augmented with  
 613 instruction-aligned 3d reconstruction, 2025. URL <https://arxiv.org/abs/2505.20279>.  
 614 3, 5, 16, 17

615

616 Rao Fu, Jingyu Liu, Xilun Chen, Yixin Nie, and Wenhan Xiong. Scene-llm: Extending language  
 617 model for 3d visual reasoning. In *2025 IEEE/CVF Winter Conference on Applications of Computer*  
 618 *Vision (WACV)*, pp. 2195–2206. IEEE, 2025. 1, 3, 8

619

620 Kaiming He, Xinlei Chen, Saining Xie, Yanghao Li, Piotr Dollár, and Ross B. Girshick. Masked  
 621 autoencoders are scalable vision learners. 2022. 19

622

623 Yining Hong, Haoyu Zhen, Peihao Chen, Shuhong Zheng, Yilun Du, Zhenfang Chen, and Chuang  
 624 Gan. 3d-llm: Injecting the 3d world into large language models. *Advances in Neural Information*  
 625 *Processing Systems*, 36:20482–20494, 2023a. 1, 3, 8

626

627 Yining Hong, Haoyu Zhen, Peihao Chen, Shuhong Zheng, Yilun Du, Zhenfang Chen, and Chuang  
 628 Gan. 3d-llm: Injecting the 3d world into large language models, 2023b. 7

629

630 Haifeng Huang, Zehan Wang, Rongjie Huang, Luping Liu, Xize Cheng, Yang Zhao, Tao Jin, and  
 631 Zhou Zhao. Chat-3d v2: Bridging 3d scene and large language models with object identifiers.  
 632 *CoRR*, 2023a. 8

633

634 Haifeng Huang, Yilun Chen, Zehan Wang, Rongjie Huang, Runsen Xu, Tai Wang, Luping Liu, Xize  
 635 Cheng, Yang Zhao, Jiangmiao Pang, et al. Chat-scene: Bridging 3d scene and large language  
 636 models with object identifiers. *Advances in Neural Information Processing Systems*, 37:113991–  
 637 114017, 2024. 1, 3, 7, 8

638

639 Jiangyong Huang, Silong Yong, Xiaojian Ma, Xiongkun Linghu, Puhao Li, Yan Wang, Qing Li,  
 640 Song-Chun Zhu, Baoxiong Jia, and Siyuan Huang. An embodied generalist agent in 3d world.  
 641 *arXiv preprint arXiv:2311.12871*, 2023b. 1, 8

642

643 Jiangyong Huang, Baoxiong Jia, Yan Wang, Ziyu Zhu, Xiongkun Linghu, Qing Li, Song-Chun Zhu,  
 644 and Siyuan Huang. Unveiling the mist over 3d vision-language understanding: Object-centric  
 645 evaluation with chain-of-analysis. In *Proceedings of the Computer Vision and Pattern Recognition*  
 646 *Conference*, pp. 24570–24581, 2025a. 8, 19

647

648 Jiangyong Huang, Xiaojian Ma, Xiongkun Linghu, Yue Fan, Junchao He, Wenxin Tan, Qing Li,  
 649 Song-Chun Zhu, Yixin Chen, Baoxiong Jia, et al. Leo-vl: Towards 3d vision-language generalists  
 650 via data scaling with efficient representation. *arXiv preprint arXiv:2506.09935*, 2025b. 1, 3

651

652 Ayush Jain, Alexander Swerdlow, Yuzhou Wang, Sergio Arnaud, Ada Martin, Alexander Sax,  
 653 Franziska Meier, and Katerina Fragkiadaki. Unifying 2d and 3d vision-language understanding.  
 654 *arXiv preprint arXiv:2503.10745*, 2025. 7, 8

648 Moo Jin Kim, Karl Pertsch, Siddharth Karamcheti, Ted Xiao, Ashwin Balakrishna, Suraj Nair,  
 649 Rafael Rafailov, Ethan Foster, Grace Lam, Pannag Sanketi, et al. Openvla: An open-source  
 650 vision-language-action model. *arXiv preprint arXiv:2406.09246*, 2024. 20  
 651

652 Bo Li, Yuanhan Zhang, Dong Guo, Renrui Zhang, Feng Li, Hao Zhang, Kaichen Zhang, Peiyuan  
 653 Zhang, Yanwei Li, Ziwei Liu, et al. Llava-onevision: Easy visual task transfer. *arXiv preprint*  
 654 *arXiv:2408.03326*, 2024. 3

655 Haoyuan Li, Yanpeng Zhou, Yufei Gao, Tao Tang, Jianhua Han, Yujie Yuan, Dave Zhenyu Chen,  
 656 Jiawang Bian, Hang Xu, and Xiaodan Liang. Does your 3d encoder really work? when pretrain-sft  
 657 from 2d vlms meets 3d vlms. *arXiv preprint arXiv:2506.05318*, 2025a. 8, 19  
 658

659 Rong Li, Shijie Li, Lingdong Kong, Xulei Yang, and Junwei Liang. Seeground: See and ground  
 660 for zero-shot open-vocabulary 3d visual grounding. In *Proceedings of the Computer Vision and*  
 661 *Pattern Recognition Conference*, pp. 3707–3717, 2025b. 7

662 Bin Lin, Yang Ye, Bin Zhu, Jiaxi Cui, Munan Ning, Peng Jin, and Li Yuan. Video-llava: Learning  
 663 united visual representation by alignment before projection. *arXiv preprint arXiv:2311.10122*,  
 664 2023. 3

665 Haotian Liu, Chunyuan Li, Yuheng Li, and Yong Jae Lee. Improved baselines with visual instruction  
 666 tuning. In *Proceedings of the IEEE/CVF conference on computer vision and pattern recognition*,  
 667 pp. 26296–26306, 2024. 3

668 Xiaojian Ma, Silong Yong, Zilong Zheng, Qing Li, Yitao Liang, Song-Chun Zhu, and Siyuan Huang.  
 669 Sqa3d: Situated question answering in 3d scenes. *arXiv preprint arXiv:2210.07474*, 2022. 2, 6, 18  
 670

671 Dominic Maggio, Hyungtae Lim, and Luca Carlone. Vggt-slam: Dense rgb slam optimized on the sl  
 672 (4) manifold. *arXiv preprint arXiv:2505.12549*, 2025. 4, 6, 18, 19

673

674 Paul McVay, Sergio Arnaud, Ada Martin, Arjun Majumdar, Krishna Murthy Jatavallabhula, Phillip  
 675 Thomas, Ruslan Partsey, Daniel Dugas, Abha Gejji, Alexander Sax, et al. Locate 3d: Real-world  
 676 object localization via self-supervised learning in 3d. In *Forty-second International Conference on*  
 677 *Machine Learning*, 2025. 7, 8, 9

678

679 OpenAI, :, Aaron Hurst, Adam Lerer, Adam P. Goucher, Adam Perelman, Aditya Ramesh, Aidan  
 680 Clark, AJ Ostrow, Akila Welihinda, et al. Gpt-4o system card, 2024. URL <https://arxiv.org/abs/2410.21276>. 5, 17

681

682

683 Kun Ouyang, Yuanxin Liu, Haoning Wu, Yi Liu, Hao Zhou, Jie Zhou, Fandong Meng, and Xu Sun.  
 684 Spacer: Reinforcing mllms in video spatial reasoning. *arXiv preprint arXiv:2504.01805*, 2025. 5

685

686 Charles R Qi, Hao Su, Kaichun Mo, and Leonidas J Guibas. Pointnet: Deep learning on point sets  
 687 for 3d classification and segmentation. In *Proceedings of the IEEE conference on computer vision*  
 688 *and pattern recognition*, pp. 652–660, 2017a. 5, 19

689

690 Charles Ruizhongtai Qi, Li Yi, Hao Su, and Leonidas J Guibas. Pointnet++: Deep hierarchical feature  
 691 learning on point sets in a metric space. *Advances in neural information processing systems*, 30,  
 692 2017b. 5, 19

693

694 Zekun Qi, Runpei Dong, Guofan Fan, Zheng Ge, Xiangyu Zhang, Kaisheng Ma, and Li Yi. Contrast  
 695 with reconstruct: Contrastive 3d representation learning guided by generative pretraining. In  
 696 *International Conference on Machine Learning*, pp. 28223–28243. PMLR, 2023a. 19

697

698 Zekun Qi, Muzhou Yu, Runpei Dong, and Kaisheng Ma. Vpp: Efficient conditional 3d generation  
 699 via voxel-point progressive representation. *Advances in Neural Information Processing Systems*,  
 700 36:26744–26763, 2023b. 19

701

Zekun Qi, Runpei Dong, Shaochen Zhang, Haoran Geng, Chunrui Han, Zheng Ge, Li Yi, and  
 702 Kaisheng Ma. Shapellm: Universal 3d object understanding for embodied interaction. In *European*  
 703 *Conference on Computer Vision*, pp. 214–238. Springer, 2024. 19

702 Zekun Qi, Wenyao Zhang, Yufei Ding, Runpei Dong, Xinqiang Yu, Jingwen Li, Lingyun Xu, Baoyu  
 703 Li, Xialin He, Guofan Fan, et al. Sofar: Language-grounded orientation bridges spatial reasoning  
 704 and object manipulation. *arXiv preprint arXiv:2502.13143*, 2025. 20

705

706 Alec Radford, Jong Wook Kim, Chris Hallacy, Aditya Ramesh, Gabriel Goh, Sandhini Agarwal,  
 707 Girish Sastry, Amanda Askell, Pamela Mishkin, Jack Clark, Gretchen Krueger, and Ilya Sutskever.  
 708 Learning transferable visual models from natural language supervision. volume 139 of *Proceedings  
 709 of Machine Learning Research*, pp. 8748–8763. PMLR, 2021. 19

710 Jonas Schult, Francis Engelmann, Alexander Hermans, Or Litany, Siyu Tang, and Bastian  
 711 Leibe. Mask3d: Mask transformer for 3d semantic instance segmentation. *arXiv preprint  
 712 arXiv:2210.03105*, 2022. 7

713 Qwen Team. Qwen2 technical report. *arXiv preprint arXiv:2407.10671*, 2024. 6

714

715 Ashish Vaswani, Noam Shazeer, Niki Parmar, Jakob Uszkoreit, Llion Jones, Aidan N Gomez, Łukasz  
 716 Kaiser, and Illia Polosukhin. Attention is all you need. *Advances in neural information processing  
 717 systems*, 30, 2017. 6

718 Fengyun Wang, Sicheng Yu, Jiawei Wu, Jinhui Tang, Hanwang Zhang, and Qianru Sun. 3d question  
 719 answering via only 2d vision-language models. *arXiv preprint arXiv:2505.22143*, 2025a. 10

720

721 Haochen Wang, Yucheng Zhao, Tiancai Wang, Haoqiang Fan, Xiangyu Zhang, and Zhaoxiang  
 722 Zhang. Ross3d: Reconstructive visual instruction tuning with 3d-awareness. *arXiv preprint  
 723 arXiv:2504.01901*, 2025b. 1, 3, 7, 8, 19

724 Jianyuan Wang, Minghao Chen, Nikita Karaev, Andrea Vedaldi, Christian Rupprecht, and David  
 725 Novotny. Vggt: Visual geometry grounded transformer. In *Proceedings of the Computer Vision  
 726 and Pattern Recognition Conference*, pp. 5294–5306, 2025c. 3, 19

727

728 Qianqian Wang, Yifei Zhang, Aleksander Holynski, Alexei A Efros, and Angjoo Kanazawa. Continuous  
 729 3d perception model with persistent state. In *Proceedings of the Computer Vision and Pattern  
 730 Recognition Conference*, pp. 10510–10522, 2025d. 19

731 Ruicheng Wang, Sicheng Xu, Yue Dong, Yu Deng, Jianfeng Xiang, Zelong Lv, Guangzhong Sun,  
 732 Xin Tong, and Jiaolong Yang. Moge-2: Accurate monocular geometry with metric scale and sharp  
 733 details. *arXiv preprint arXiv:2507.02546*, 2025e. 6, 18, 19

734

735 Diankun Wu, Fangfu Liu, Yi-Hsin Hung, and Yueqi Duan. Spatial-mllm: Boosting mllm capabilities  
 736 in visual-based spatial intelligence. *arXiv preprint arXiv:2505.23747*, 2025a. 3, 5

737

738 Xiaoyang Wu, Yixing Lao, Li Jiang, Xihui Liu, and Hengshuang Zhao. Point transformer v2:  
 739 Grouped vector attention and partition-based pooling. *Advances in Neural Information Processing  
 740 Systems*, 35:33330–33342, 2022. 5, 19

741

742 Xiaoyang Wu, Li Jiang, Peng-Shuai Wang, Zhijian Liu, Xihui Liu, Yu Qiao, Wanli Ouyang, Tong  
 743 He, and Hengshuang Zhao. Point transformer v3: Simpler faster stronger. In *Proceedings of the  
 744 IEEE/CVF conference on computer vision and pattern recognition*, pp. 4840–4851, 2024. 4, 5, 6,  
 745 19

746

747 Xiaoyang Wu, Daniel DeTone, Duncan Frost, Tianwei Shen, Chris Xie, Nan Yang, Jakob Engel,  
 748 Richard Newcombe, Hengshuang Zhao, and Julian Straub. Sonata: Self-supervised learning of  
 749 reliable point representations. In *Proceedings of the Computer Vision and Pattern Recognition  
 750 Conference*, pp. 22193–22204, 2025b. 4, 5, 6, 19

751

752 Jihan Yang, Shusheng Yang, Anjali W Gupta, Rilyn Han, Li Fei-Fei, and Saining Xie. Thinking in  
 753 space: How multimodal large language models see, remember, and recall spaces. In *Proceedings  
 754 of the Computer Vision and Pattern Recognition Conference*, pp. 10632–10643, 2025. 3, 5, 8, 16,  
 755 20

756

757 Chandan Yeshwanth, Yueh-Cheng Liu, Matthias Nießner, and Angela Dai. Scannet++: A high-  
 758 fidelity dataset of 3d indoor scenes. In *Proceedings of the IEEE/CVF International Conference on  
 759 Computer Vision*, pp. 12–22, 2023. 8, 16

756 Hanxun Yu, Wentong Li, Song Wang, Junbo Chen, and Jianke Zhu. Inst3d-lmm: Instance-aware 3d  
 757 scene understanding with multi-modal instruction tuning. In *Proceedings of the Computer Vision*  
 758 and *Pattern Recognition Conference*, pp. 14147–14157, 2025. 3, 7

759

760 Xiaohua Zhai, Basil Mustafa, Alexander Kolesnikov, and Lucas Beyer. Sigmoid loss for language  
 761 image pre-training. In *Proceedings of the IEEE/CVF international conference on computer vision*,  
 762 pp. 11975–11986, 2023. 6

763 Wenyao Zhang, Hongsi Liu, Zekun Qi, Yunnan Wang, Xinqiang Yu, Jiazhao Zhang, Runpei Dong,  
 764 Jiawei He, He Wang, Zhizheng Zhang, et al. Dreamvla: a vision-language-action model dreamed  
 765 with comprehensive world knowledge. *arXiv preprint arXiv:2507.04447*, 2025. 20

766

767 Yiming Zhang, ZeMing Gong, and Angel X Chang. Multi3drefer: Grounding text description to  
 768 multiple 3d objects. In *Proceedings of the IEEE/CVF International Conference on Computer*  
 769 *Vision*, pp. 15225–15236, 2023. 6, 18

770 Yuanhan Zhang, Jinming Wu, Wei Li, Bo Li, Zejun Ma, Ziwei Liu, and Chunyuan Li. Video  
 771 instruction tuning with synthetic data. *arXiv preprint arXiv:2410.02713*, 2024. 6

772

773 Hengshuang Zhao, Li Jiang, Jiaya Jia, Philip HS Torr, and Vladlen Koltun. Point transformer. In  
 774 *Proceedings of the IEEE/CVF international conference on computer vision*, pp. 16259–16268,  
 775 2021. 5, 19

776 Duo Zheng, Shijia Huang, and Liwei Wang. Video-3d lilm: Learning position-aware video represen-  
 777 tation for 3d scene understanding. In *Proceedings of the Computer Vision and Pattern Recognition*  
 778 *Conference*, pp. 8995–9006, 2025. 1, 2, 3, 4, 7, 8

779

780 Enshen Zhou, Jingkun An, Cheng Chi, Yi Han, Shanyu Rong, Chi Zhang, Pengwei Wang, Zhongyuan  
 781 Wang, Tiejun Huang, Lu Sheng, et al. Roborefer: Towards spatial referring with reasoning in  
 782 vision-language models for robotics. *arXiv preprint arXiv:2506.04308*, 2025. 1

783 Chenming Zhu, Tai Wang, Wenwei Zhang, Kai Chen, and Xihui Liu. Scanreason: Empowering 3d  
 784 visual grounding with reasoning capabilities. In *European Conference on Computer Vision*, pp.  
 785 151–168. Springer, 2024a. 3, 7

786 Chenming Zhu, Tai Wang, Wenwei Zhang, Jiangmiao Pang, and Xihui Liu. Llava-3d: A simple  
 787 yet effective pathway to empowering lmms with 3d-awareness. *arXiv preprint arXiv:2409.18125*,  
 788 2024b. 1, 2, 3, 4, 7, 8

789

790 Ziyu Zhu, Xiaoqian Ma, Yixin Chen, Zhidong Deng, Siyuan Huang, and Qing Li. 3d-vista: Pre-trained  
 791 transformer for 3d vision and text alignment, 2023. 7

792

793 Ziyu Zhu, Zhuofan Zhang, Xiaoqian Ma, Xuesong Niu, Yixin Chen, Baoxiong Jia, Zhidong Deng,  
 794 Siyuan Huang, and Qing Li. Unifying 3d vision-language understanding via prompttable queries.  
 795 *ECCV*, 2024c. 7

796

797

798

799

800

801

802

803

804

805

806

807

808

809

810 A ADDITIONAL DATASET DETAILS  
811812 Grounding Chain-of-Thought Dataset plays a crucial role in our training, guiding the model to learn  
813 how to incorporate 3D visual grounding as an intermediate step in spatial reasoning. Here, we provide  
814 additional details on the dataset construction.  
815816 A.1 INSTRUCTION QA GENERATION  
817818 We first construct spatial reasoning QA pairs without chain-of-thought annotations, following the  
819 dataset generation pipeline of (Yang et al., 2025; Fan et al., 2025). All data are sourced from existing  
820 large-scale 3D datasets, including ScanNet (Dai et al., 2017), ScanNet++ (Yeshwanth et al., 2023),  
821 and ARKitScenes (Baruch et al., 2021). To ensure consistency across datasets, we perform the  
822 following preprocessing steps for each scene:  
823824 

- **Point Cloud.** We directly use the raw point cloud provided by each dataset. Since ScanNet++  
825 and ARKitScenes do not guarantee alignment of the global coordinate system with the physical  
826 room structure (e.g., the XY plane may not align with walls or floors), we further apply axis  
827 alignment. Specifically, we estimate the gravity direction and compute the principal components  
828 of the point cloud to align the axes, yielding a transformation matrix for each scene.
- **Sampled Frame Data.** we uniformly sample 50 RGB frames, which serve as the basis for  
829 constructing frame metadata. These frames provide a consistent visual context for generating  
830 spatial reasoning questions and ensure coverage of diverse viewpoints within the scene.  
831

832 Based on the preprocessed data, we further construct detailed metadata for each scene, consisting of  
833 the following components:  
834835 

- **Scene Metadata.** This metadata is used for all spatial reasoning questions construction. We  
836 extract the axis-aligned bounding boxes (AABBs) of all object instances, either directly from  
837 mask annotations or by converting from oriented bounding box (OBB) annotations. In addition  
838 to bounding boxes, this metadata also includes global scene statistics such as the number of  
839 objects and room dimensions, which are later used to formulate numerical reasoning questions.
- **Frame Metadata.** This metadata is used specifically for appearance-based temporal reasoning  
840 questions. For each object, we determine its appearance time by recording the first frame  
841 in which its 2D mask area exceeds a given threshold. Consequently, the frame metadata of  
842 each scene contains the appearance time of all objects, enabling the construction of reasoning  
843 questions grounded in temporal visual evidence.  
844

845 These two types of metadata provide the necessary information to generate a diverse set of spatial  
846 and temporal reasoning questions. Following the predefined question templates in (Yang et al.,  
847 2025), we iterate over the scene metadata to construct a large pool of candidate questions and their  
848 corresponding answers. The detailed procedures are as follows:  
849850 **Spatial Reasoning QA.**  
851852 

- **Object Count.** For each object category with at least two instances in the scene, we generate  
853 counting questions by directly querying the number of instances.
- **Absolute Distance.** We randomly select pairs of objects that appear only once in the scene and  
855 compute their Euclidean distance, which serves as the basis for absolute distance queries.
- **Object Size.** For objects with a single instance, we compute the object size using the diagonal  
857 length of their AABB, and use this value to construct size-related questions.
- **Room Size.** We estimate the overall room size of each scene using the alpha-shape algo-  
859 rithm applied to the scene point cloud, allowing us to ask questions about scene-level spatial  
860 dimensions.
- **Relative Distance.** We randomly select a set of  $N$  objects ( $3 \leq N \leq 5$ ), compute all pairwise  
863 distances, and identify the closest pair of objects. This enables the construction of questions that  
require comparative spatial reasoning.

864 • **Relative Direction.** We randomly select three objects with unique instances and compute their  
 865 relative directions based on the centers of their AABBs. The resulting orientation relations form  
 866 the basis of direction-based reasoning questions.  
 867

868 **Temporal Reasoning QA.** For temporal reasoning (i.e., appearance order), we randomly select four  
 869 objects from each scene and determine their order of appearance using the frame metadata.  
 870

871 **Route Planning QA.** For route planning questions, we follow the procedure in VLM-3R (Fan et al.,  
 872 2025) and employ the Habitat simulator to generate diverse navigation trajectories between two  
 873 predefined points in each scene. The turning direction at each step is determined by computing  
 874 the angle between consecutive anchor points along the trajectory. To identify relevant objects, we  
 875 calculate their proximity to the trajectory by measuring the distance between anchor points and the  
 876 3D bounding boxes of scene objects provided in the scene metadata. Finally, we construct the QA  
 877 pairs using predefined templates consistent with those in VLM-3R (Fan et al., 2025), where each  
 878 question is grounded in the trajectory’s turning direction and nearby objects.  
 879

## 880 A.2 CHAIN-OF-THOUGHT GENERATION

881 Building upon the generated QA pairs and their associated 3D object bounding boxes, we further  
 882 create CoT annotations to guide the model in exploiting 3D visual grounding for spatial reasoning.  
 883 Specifically, we employ GPT-4o (OpenAI et al., 2024) to generate CoT reasoning paths for each QA  
 884 pair. To mitigate potential hallucinations from the LLM, we construct a bird’s-eye-view map of each  
 885 scene using the preprocessed point cloud. On this map, we explicitly annotate the 3D bounding boxes  
 886 of relevant objects, with different colors denoting distinct object categories, consistent with the color  
 887 keys used in the input bounding box information. The BEV map, together with the question, answer,  
 888 and relevant object annotations, is then provided to GPT-4o to generate coherent and detailed CoT  
 889 paths. For efficiency, we exclude tasks that do not require complex spatial reasoning or grounding  
 890 (e.g., Room Size, Object Count, Appearance Order) from CoT generation, as these can be accurately  
 891 answered without the need for step-by-step grounding-based reasoning.  
 892

## 893 A.3 DATA FORMAT

894 To train a model that can determine when to ground relevant objects and perform step-by-step  
 895 reasoning autonomously, we prepend a *question analysis* part to each answer. This part explicitly  
 896 guides the model to decide whether grounding is required before initiating the reasoning process. An  
 897 example of the final data format for QA pairs with CoT is shown below:  
 898

### 900 QA w/ CoT Example

901 Question: [preprompt] If I am standing by the radiator and facing the table, is the telephone  
 902 to the left or the right of the table? Options: A. left B. right

903 Answer: <think>The question is asking for the relative direction of the telephone  
 904 with respect to my position (at the radiator) while facing the table. To solve this, I can  
 905 identify all relevant objects and their bounding boxes first.

906 radiator 1 <bbox>(-1.9165, -1.0266, 0.0798, -1.6415, 0.9513, 0.6104)</bbox>, table  
 907 1 <bbox>(-0.9128, -1.7861, 0.0150, -0.5043, -1.0341, 0.5050)</bbox>, telephone 1  
 908 <bbox>(-1.4182, 0.9637, 0.9736, -1.1277, 1.2378, 1.0825)</bbox>

909 To determine the telephone’s position relative to the table, I analyze spatial relationships through three steps:  
 910

911 Step 1: Observer Position and Orientation

912 Standing at the radiator’s centroid:

913 - x = (-1.9165 + -1.6415)/2 = -1.779  
 914 - y = (-1.0266 + 0.9513)/2 = -0.038

915 Facing the table, whose centroid: ..

916 The telephone lies to the left of the table. Option A is correct. </think>  
 917 <answer>A</answer>

918 And example of the final data format for QA pairs without CoT is shown below:  
 919

920 QA w/o CoT Example  
 921

922 Question: [preprompt] What is the size of this room (in square meters)? If multiple rooms  
 923 are shown, estimate the size of the combined space.  
 924

925 Answer: <think>The question is asking for the room size in square meters. To  
 926 solve this, I can rely on the overall spatial information present in the video without identifying  
 927 any object bounding boxes.  
 928

From the video, the room size is about 11.0 m<sup>2</sup>.</think>  
 929 <answer>11.0</answer>  
 930

931 By structuring the data in this way, the model learns to autonomously decide when to ground relevant  
 932 objects and perform step-by-step reasoning, without the need for additional prompting.  
 933

934 B ADDITIONAL IMPLEMENTATION DETAILS  
 935

936 B.1 TRAINING DETAILS  
 937

938 GS-Reasoner is trained end-to-end with cross-entropy loss for next-token prediction. We first  
 939 pretrain on subsets of 3D visual grounding datasets, including ScanRefer (Chen et al., 2020),  
 940 Multi3DRef (Zhang et al., 2023), SR3D, and NR3D (Achlioptas et al., 2020), to warm up ob-  
 941 ject grounding, and then finetune on our proposed GCoT dataset, the remaining grounding data, and  
 942 other 3D tasks (ScanQA (Azuma et al., 2022), SQA3D (Ma et al., 2022), Scan2Cap (Chen et al.,  
 943 2021)). All parameters are learnable except those of the vision encoder. The LLM learning rate is  
 944 fixed at  $1e^{-5}$ , while other modules use  $1e^{-4}$  during pretraining and  $1e^{-5}$  during finetuning. We use a  
 945 batch size of 16 for pretraining and 256 for finetuning, set  $K = 64$  in all experiments, and uniformly  
 946 sample  $N \in [16, 48]$  images per scene during training. Data augmentation is crucial for training  
 947 GS-Reasoner, as the autoregressive objective tends to overfit object grounding under limited 3D data.  
 948 We avoid conventional point cloud augmentations (e.g., jittering, elastic distortion) already covered  
 949 in Sonata’s pretraining, and instead focus on decoupling geometric and positional cues. Specifically,  
 950 we apply Z-axis rotations of  $[90^\circ, 180^\circ, 270^\circ]$ , random scaling within  $[0.75, 1.25]$ , and translations  
 951 within  $[-1, 1]$  meters, which alter bounding box positions and scales, forcing the model to exploit  
 952 both cues for accurate predictions.  
 953

954 B.2 INFERENCE DETAILS  
 955

956 We develop a pipeline to recover metric depth and camera parameters from multi-view images,  
 957 enabling spatial reasoning without any input beyond images. Specifically, we first use VGGT-  
 958 SLAM (Maggio et al., 2025) to reconstruct dense depth maps and relative camera intrinsics and  
 959 extrinsics from the multi-view images. We then apply MoGe-2 (Wang et al., 2025e) to estimate  
 960 absolute-scale depth maps and per-image camera intrinsics independently. Since the intrinsics from  
 961 these two methods may not be aligned, we avoid direct scale estimation in the depth dimension.  
 962 Instead, we project all points into the camera coordinate system and compute a global scale factor  
 963  $s$  such that the scaled VGGT-SLAM point maps align with the corresponding MoGe-2 point maps  
 964 across all views. Formally,  $s$  is obtained by solving the following optimization problem:  
 965

$$s^* = \arg \min_{s>0} \sum_{i=1}^N \sum_{j=1}^{M_i} \|s \cdot p_{i,j}^{\text{VGGT-SLAM}} - p_{i,j}^{\text{MoGe-2}}\|^2, \quad (3)$$

966 where  $p_{i,j}^{\text{VGGT-SLAM}}$  and  $p_{i,j}^{\text{MoGe-2}}$  denote the  $j$ -th point in the  $i$ -th view from VGGT-SLAM and MoGe-  
 967 2, respectively,  $M_i$  is the number of valid points in view  $i$ , and  $N$  is the total number of views.  
 968 Furthermore, we compute a per-scene axis-alignment transformation matrix based on the estimated  
 969 camera poses and reconstructed point clouds.  
 970

## 972 C ADDITIONAL RELATED WORK

974 **Point Cloud Representation Learning.** Point cloud representation learning has been extensively  
 975 studied for 3D understanding. Early works like PointNet (Qi et al., 2017a;b) use MLPs and sym-  
 976 metric functions to extract global features from point clouds. More recent methods, such as Point  
 977 Transformer (Zhao et al., 2021; Wu et al., 2022; Qi et al., 2023b; Wu et al., 2024; 2025b), leverage  
 978 attention mechanisms to capture local geometric structures and point relationships. ACT (Dong et al.,  
 979 2022) pioneers cross-modal geometry understanding through 2D or language foundation models such  
 980 as CLIP (Radford et al., 2021) or MAE (He et al., 2022). RECON (Qi et al., 2023a; 2024) further  
 981 proposes a learning paradigm that unifies generative and contrastive learning. Despite architectural  
 982 differences, these methods share a common pipeline: points are grouped based on spatial distribution,  
 983 features are extracted per group, and then aggregated into a global representation. The resulting  
 984 sparse features can be upsampled to the original resolution for tasks such as semantic segmentation.

## 985 D ADDITIONAL EXPERIMENTAL ANALYSIS AND RESULTS

### 986 D.1 ANALYSIS ON GENERAL 3D TASKS

987 As shown in Tab. 3, GS-Reasoner does not achieve leading results on ScanQA and SQA3D. We  
 988 believe the main reasons are the presence of many ambiguous questions in these datasets that do  
 989 not clearly specify the target object, as well as a strong bias in answer distribution. These factors  
 990 encourage the model to overfit to textual patterns instead of effectively exploiting 3D tokens. Recent  
 991 studies (Huang et al., 2025a; Li et al., 2025a) have also shown that finetuning LLMs without 3D  
 992 input can yield results comparable to the state of the art on ScanQA and SQA3D. Incorporating  
 993 reconstruction constraints in the output (as done in ROSS3D (Wang et al., 2025b)) may help encourage  
 994 the model to utilize 3D tokens, and we leave this for future research.

995 Table 9: **Ablation study on the impact of predicted depth maps and poses on spatial reasoning.**

1000	Recon. Methods	Align Methods	Numerical Question					Multiple-Choice Question			
			Avg.	Obj. Cnt.	Abs. Dist.	Obj. Size	Room Size	Rel. Dist.	Rel. Dir.	Route Plan	Appr. Order
1001	-	-	70.1	70.9	73.6	77.8	81.8	70.6	90.5	42.8	52.6
1002	VGGT-SLAM	MoGe-2	64.7	69.1	61.9	70.0	65.7	65.4	88.9	44.3	52.3
1003	VGGT-SLAM	GT-Depth	67.8	69.4	68.9	76.5	78.8	65.2	87.6	43.4	52.9
1004	VGGT	MoGe-2	59.6	66.8	55.6	65.5	63.1	58.3	77.3	34.0	51.6
1005	CUT3R	-	56.8	66.8	55.3	60.2	50.7	59.8	76.6	34.0	50.7
1006	TTT3R	-	58.0	67.5	57.6	60.2	46.5	62.8	82.9	35.1	51.5

### 1008 D.2 ABLATION STUDY ON PREDICTED DEPTH MAPS AND POSES

1009 We further evaluate the impact of different depth and pose estimation methods on the final spatial  
 1010 reasoning performance. Specifically, we consider the following geometry reconstruction methods:  
 1011 VGGT-SLAM (Maggio et al., 2025), VGGT (Wang et al., 2025c), CUT3R (Wang et al., 2025d), and  
 1012 TTT3R (Chen et al., 2025). For relative geometry reconstruction methods (VGGT-SLAM, VGGT),  
 1013 we use MoGe-2 (Wang et al., 2025e) for absolute scale recovery. We also experiment with using  
 1014 ground-truth depth for absolute scale recovery. The results are shown in Tab. 9, where the first row  
 1015 corresponds to using ground-truth depth and poses. From the experiments, we summarize two key  
 1016 factors that influence performance:

- 1017 • **Accuracy of metric scale.** As observed, the most significant performance drop compared to  
 1018 using ground truth depth occurs in tasks related to absolute size estimation, such as room  
 1019 size and object absolute distance. During training, GS-Reasoner utilizes ground truth depth,  
 1020 which leads the model to prioritize 3D features in the input for these tasks. Consequently,  
 1021 inaccuracies in metric scale have a substantial impact on the results of such tasks. Notably,  
 1022 when using ground truth depth instead of MoGe2-predicted depth for metric alignment,  
 1023 there is a significant performance improvement.
- 1024 • **Accuracy of pose.** The accuracy of pose affects the relative positional distribution of object  
 1025 point clouds within the scene, thereby influencing the model’s understanding of spatial

relationships between objects. In the point clouds estimated by CUT3R, we observed significant pose errors, often resulting in completely incorrect scene layouts. This leads to a noticeable decline in GS-Reasoner’s performance on tasks such as object relative direction. TTT3R improves upon CUT3R by reducing pose error accumulation during long-sequence inputs, resulting in some performance gains.

Beyond these two factors, other aspects have a relatively minor impact on spatial reasoning. For instance, the quality of depth details (e.g., sharpness) does not significantly affect GS-Reasoner.

### D.3 MORE QUALITATIVE RESULTS

We present qualitative results of GS-Reasoner on VSI-Bench (Yang et al., 2025) as follows:



Figure 4: Qualitative results on VSI-Bench.

## E FUTURE WORK

Spatial reasoning is a key aspect of robotics and embodied reasoning, especially for the vision-language-action (VLA) models (Kim et al., 2024; Qi et al., 2025; Zhang et al., 2025). Leveraging the strong spatial reasoning ability of GS-Reasoner in robotic tasks can substantially enhance the generalization and robustness of embodied reasoning. Future directions include jointly fine-tuning with GCoT data and action data, and employing GS-Reasoner as an embodied brain for planning and task decomposition.

## F THE USE OF LARGE LANGUAGE MODELS (LLMs)

In this work, we leverage LLMs to facilitate the construction of our *Grounded Chain-of-Thought (GCOT)* dataset. Specifically, the generation of CoT paths for spatial reasoning tasks is performed using LLMs, which allows us to capture rich intermediate reasoning steps that go beyond simple question-answer pairs.

1080

1081

1082

1083

1084

1085

1086

1087

1088

1089

1090

1091

1092

1093

1094

1095

1096

1097

1098

1099

1100

1101

1102

1103

1104

1105

1106

1107

1108

1109

1110

1111

1112

1113

**Question**

If I am standing by the **stove** and facing the **sofa**, is the **tv** to my front-left, front-right, back-left, or back-right?  
 The directions refer to the quadrants of a Cartesian plane (if I am standing at the origin and facing along the positive y-axis).

- A. front-left
- B. back-right
- C. back-left
- D. front-right

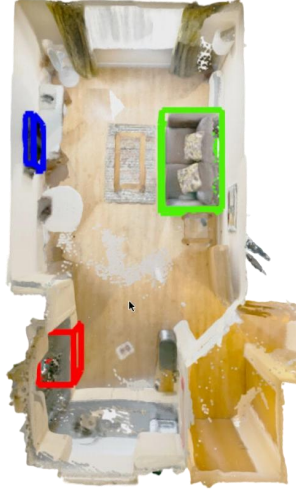
**GS-Reasoner**

<think>The question asks for the TV's relative direction from my position (at the stove) while facing the sofa. I can find these objects as follows first:  
 stove 1 `<bbox>(-1.8902, -1.7634, -1.0509, -1.3120, -0.9420, -0.1400)</bbox>`, sofa 1 `<bbox>(0.2240, 1.1322, -1.0505, 1.2367, 2.8400, -0.2070)</bbox>`, tv 1 `<bbox>(-1.9141, 1.7940, 0.0661, -1.8002, 2.5420, 0.6670)</bbox>`

The relative direction can be determined by the local coordinates of the TV, calculated in 3 steps:

Step 1: Observer frame  
 Stove centroid (observer): (-1.601, -1.353), Sofa centroid: (0.730, 1.986), Facing vector: (2.332, 3.339), normalized  $\rightarrow$  forward = (0.574, 0.822), Right vector = (0.822, -0.574)  
 Step 2: TV position  
 TV centroid: (-1.857, 2.168), Vector (observer  $\rightarrow$  TV): (-0.256, 3.521)  
 Step 3: Projection to local coordinates  
 $x_{local} = -2.269$ ,  $y_{local} = 2.760$ .  $y_{local} > 0 \rightarrow$  front;  $x_{local} < 0 \rightarrow$  left. Among options A is correct.</think>

<answer>A</answer>

**Figure 5: Qualitative results on VSI-Bench.****Question**

Measuring from the closest point of each object, which of these objects (**clock**, **monitor**, **trash bin**, **window**) is the closest to the **door**?

- A. clock
- B. monitor
- C. trash bin
- D. window

**GS-Reasoner**

<think>The question asks which object (clock, monitor, trash bin, window) is closest to the door. I can find these objects as follows first:  
 door 1 `<bbox>(-0.9532, -1.7846, -0.6190, -0.0280, -1.7050, 1.8800)</bbox>`, clock 1 `<bbox>(-1.4201, -0.2318, 2.0500, -1.3635, 0.0800, 2.3851)</bbox>`, monitor 1 `<bbox>(-1.3001, 0.3504, 0.8650, -1.1550, 0.8770, 1.2751)</bbox>`, trash bin 1 `<bbox>(-1.2300, 0.9840, -0.0309, -0.8100, 1.2350, 0.3450)</bbox>`, window 1 `<bbox>(-1.3400, 1.7945, 0.7600, 1.6420, 2.1580, 2.5025)</bbox>`

The closest object can be determined by the minimum distance to the door, calculated as:

distance =  $\sqrt{gx^2 + gy^2 + gz^2}$  Calculations:  
 - Clock  $\rightarrow$  gx = 0.410, gy = 1.474, gz = 0.170  $\rightarrow$  dist = 1.540  
 - Monitor  $\rightarrow$  gx = 0.202, gy = 2.055, gz = 0.000  $\rightarrow$  dist = 2.065  
 - Trash bin  $\rightarrow$  gx = 0.000, gy = 2.689, gz = 0.000  $\rightarrow$  dist = 2.689  
 - Window  $\rightarrow$  gx = 0.000, gy = 3.499, gz = 0.000  $\rightarrow$  dist = 3.499

Conclusion: Clock is closest to the door. Among options, A is correct.

</think>

<answer>A</answer>

**Figure 6: Qualitative results on VSI-Bench.**

1131

1132

1133

1134

1135

1136

1137

1138

1139

1140

1141

1142

1143

1144

1145

1146

1147

1148

1149

1150

1151

1152

1153

1154

1155

1156

1157



1158

1159

1160

1161

1162

1163

1164

1165

1166

1167

1168

1169

1170

1171

1172

1173

1174

1175

1176

1177

1178

1179

1180

1181

1182

1183

1184

1185

1186

1187

**Question**

What is the length of the longest dimension (length, width, or height) of the **bed**, measured in centimeters?

**GS-Reasoner**

<think>The question is asking for the size of the bed. To solve this, I can identify the bounding box for bed first.  
 bed 1 <bbox>(-1.4802, -0.3567, -0.0079, -0.3591, 1.9101, 1.0911)</bbox>  
 The bounding box for the bed is given in meters. Calculating dimensions:  
 \* Length (x-axis):  $-0.3591 - (-1.4802) = 1.1211$  m  
 \* Width (y-axis):  $1.9101 - (-0.3567) = 2.2668$  m  
 \* Height (z-axis):  $1.0911 - (-0.0079) = 1.0990$  m  
 The longest dimension is width (2.2668 m). Convert to cm:  $2.2668 * 100 = 226.68$  cm  $\approx 227$  cm</think>  
 <answer>227</answer>

Figure 7: Qualitative results on VSI-Bench.